Secondary carbides in high chromium cast irons: an alternative approach to their morphological and spatial distribution characterization

M.Agustina Guitar[1,a], Anna Scheid[1], Sebastián Suárez[1], Dominik Britz[1,2], Martín Duarte Guigou[3,4], Frank Mücklich[1,2]

[1]Department of Materials Science, Saarland University. Campus D3.3, D-66123, Saarbrücken, Germany.
[2]Materials Engineering Centre Saarland. Campus D3.3, D-66123, Saarbrücken, Germany.
[3] Programa de Ingeniería de Materiales, Facultad de Ingeniería y Tecnologías, Universidad Católica del Uruguay, Av. 8 de Octubre 2738 - CP 11600, Montevideo, Uruguay.
[4] Laboratorio de Desarrollo de Nuevos Materiales, Tubacero S.A., Cnel. Raíz 949 - CP12900, Montevideo, Uruguay.

[a] a.guitar@mx.uni-saarland.de

Abstract

Secondary carbides precipitated in high chromium cast irons during thermal treatments were characterized by means of different characterization techniques, including scanning electron microscopy, energy dispersive X-ray spectroscopy, electron backscattered diffraction and a combination of chemical etching with confocal scanning laser microscopy. This set of techniques provides a full morphological, chemical and crystallographic description of the analysed phases.

This work evaluated different methods for optimizing the image acquisition for a further image analysis (IA) based on the threshold binarization. Finally, the carbide size, distribution and morphology were determined after IA of the images acquired by aforementioned characterization techniques. Although the different techniques report some dispersion in the value for the average particle size, the particle inter-spacing and aspect ratio meet within the error value. The proposed characterization methodology provides statistically reliable data for a further evaluation of related physical properties in composites.

Keywords: secondary carbides; morphological characterization; high chromium cast irons

1.- Introduction

It is widely acknowledged that the factors which influence the mechanical response of composite materials are vast, such as: the processing method, microstructure and properties of the matrix, and size and distribution of second phase particles [1]. Microstructural evolution (i.e. grain size and growth rate) can be controlled by the size, distribution and volume fraction of second phase particles, which might act as pinning centre for the grain boundary mobility [1]. Additionally, the presence of a large amount of finely dispersed second-phase particles would further act as pinning centres for mobile dislocations segments, which results in an improvement of the mechanical response of the system by a dispersion-strengthening effect [2]. One clear example of how the microstructure and the presence of second-phase precipitates influence the properties of the materials are creep-resistant steels, whose microstructure degradation is given by the agglomeration and coarsening of precipitated as well as their morphological changes [2,3]. The agglomeration process leads to the decrease in the amount of pinning centres, increasing the interparticle spacing and thus, reducing an effective dislocation hindering. The precipitation of fine carbides can severely restrict or avoid altogether grain growth during stress relief treatments or recrystallization processes in steels [4].

Carbides precipitation is an important strengthening mechanism usually denominated secondary hardening [5,6]. Allowing the precipitation of finely dispersed cementite particles has been observed to improve the work hardening rate in ultrafine-grained steels. The fine carbide particles act as obstacles for grain boundary migration during the deformation and subsequent annealing treatment as result of a Zener boundary drag effect [5,7]. The volume fraction and distribution of the carbide particles play a fundamental role in this process, since a very fine carbide dispersion can even suppress the primary recrystallization, favouring the sub-grain formation or a polycrystalline grain structure as a result of the accumulation of dislocations at sub-grain boundaries [7]. Moving grain boundaries will be attached to the particles and its motion restricted by a drag force exerted by the particles which is proportional to particle radius (r) and volume fraction of the second phase particles (r/f) [8]. Furthermore, the shape of the particles is also an important parameter to be evaluated, since the arrangement of non-spherical precipitates has also an influence in the pinning force and thus, in the material response [8].

Qualitative and quantitative characterization of second phase particles precipitated within a metallic matrix can be performed by merging different characterization techniques, together with subsequent image analysis. Optical microscopy has been the mostly used technique for metallographic characterization of metals, however, its limited magnification and resolution severely hinders the detection of sub-micron size particles [9]. A more recently developed technique, such the confocal laser scanning microscope (CLSM) combines high-resolution optical imaging with depth selectivity and

allows the detection of sub-micron size features. It has been used for the characterization of biological samples [10,11], microstructural changes in foods [12] and mineral rocks [13]. However, only during the last decade, this technique has been incorporated in the metallurgical field for studying fracture process in steels and alloys [14]. The use of chemical etching together with CLSM is proposed in this work for the characterization of second phase particles by the construction of three-dimensional topographic maps. Scanning electron microscope (SEM) overcomes the shortages in the spatial resolution of optical and laser microscopes [9]. By using the backscattered (BSE) acquisition mode, the atomic number contrast is enhanced as a function of the number of backscattered electrons, allowing the detection of different phases in a specimen. On the other hand, energy dispersive spectrometry (EDS) detects the X-ray emitted from the surface of a sample and thus, the chemical composition of different phases can be qualitatively evaluated [9]. Electron backscatter diffraction (EBSD) enables individual grain orientations, local texture, point-to point orientation correlations, and phase identification and distributions to be determined on the surfaces of bulk polycrystals. The application has experienced rapid acceptance in metallurgical and materials science laboratories. The sample preparation from the bulk is relatively easy to perform, it offers high speed of data acquisition, and the access to complementary information about the microstructure on a submicron scale [15]. These techniques have been widely used, separately or combined, for the detection and characterization of carbides or second phase particles [16–18].

The objective of this work is to propose a guide for the systematic characterization of second phase particles by combining a variety of techniques such as SEM, EDS, CLSM and EBSD. As a particular case, the characterization of secondary carbides precipitated during thermal treatments in high chromium cast iron (HCCI) containing 16 %Cr is presented. This material can be considered as a composite material, since it shows a structure composed of large eutectic M_7C_3 carbides in a softer iron matrix, which is austenite in the as-cast condition or martensite after a subsequent thermal treatment [19,20], where the precipitation of secondary carbides occurs within the matrix. Since the morphologies of secondary carbides and crystallographic properties of the matrix are the predominant characteristics influencing the hardness and wear behaviour of the alloy [22], it is of high relevance the quantitative analysis and degree of distribution of secondary carbides. This includes the chemical and crystallographic identification and determination of size, distribution and particle shape of the carbides by quantitative metallography.

2.- Experimental

The material analysed is high chromium cast iron (HCCI) with a Cr content of approx. 16 wt.%. The samples were manufactured in an arc furnace and casted into cubic sand moulds. The chemical composition was determined by emission spectroscopy methods using a GNR Metal Lab 75/80 Optical Emission Spectroscope. The chemical composition in weight fraction is given in table 1.

Table 1: Chemical composition (weight fraction) of the tested materials.

C%	Si%	Mn%	Cr%	Ni%	Mo%	S%	P%	Cu%
2.43	0.47	0.76	15.84	0.17	0.41	0.02	0.02	0.04

The as-cast material was subsequently heat treated in order to tailor the microstructure. The thermal treatment consisted in a destabilization step at 980 °C for 1.5 hours followed by a sub-critical diffusion (SCD) at 650 °C for 12 h and furnace cooled until room temperature. A final quenching (Q) step (isothermal treatment at 980 °C for 1.5 h and subsequent air quenching) leads to a martensitic microstructure. The schematic representation of the SCD+Q treatment is shown in Figure 1.

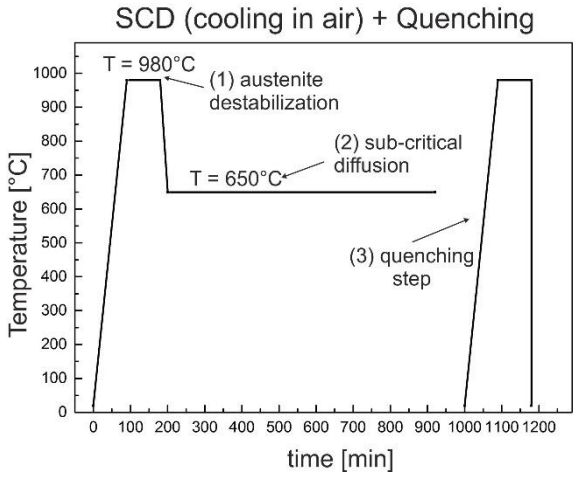

Figure 1: schematic representation of the SCD+Q treatment

The sample preparation consisted of grinding with SiC paper and polishing with diamond suspensions up to 1 µm for microscopy analysis, and up to oxide polishing suspension OPS (mean particle size: 50 nm) for EBSD analysis. Details of the polishing process are shown in Table 2. In order to correlate the analysis performed with different techniques, three regions of interest (100 x 100 μm^2 each one) was delimited with crosses made using a focus ion beam.

Table 2: Parameters for the samples metallographic preparation

Grinding/Polishing pads	Grain size	Time
SiC paper	#600 - #1200	3 minutes each
MD Dac	6 µm diamond suspension	5 minutes
MD Mol	3 µm Diamond suspension	5 minutes

MD Nap	1 µm Diamond suspension	5 minutes
MD Chem	OPS (50 nm)	4 minutes (+4 minutes water)

The samples microstructure was analysed using a FEI Helios NanoLab field emission scanning electron microscope (FE-SEM) with an acceleration voltage of 10 kV and a 1.4 nA beam current. A high sensitivity solid-state backscattered electrons detector (vCD) was used for better contrast between the phases, by detecting variations in their chemical composition (different atomic number). The carbides chemistry and crystallography were identified using EDS at 15 kV accelerating voltage and EBSD at 20kV and 11 nA, respectively. EBSD measurements were done using step sizes of 80 and 20 nm and the analysis of the data was performed using EDAX TSL OIM data analysis system. The EBSD data post-processing consisted of the application of a confidence index (CI) standardization routine and the filtering of the data possessing a CI below 0.09.

The samples were analysed using a confocal laser scanning microscopy (CLSM) with 100x objectives after etching with Vilella etchant (1g picric acid, 5 ml HCl, 100 ml C_2H_6O) at room temperature for 10 seconds for the exposure of the secondary carbides from the matrix. Carbides size, distribution and morphology were determined from SEM and CLSM images by image analysis (IA) using the A4i© (aquinto AG) software and FIJI [24] image processing package from ImageJ open access software.

2.1.- Optimization of techniques

Contrast analysis

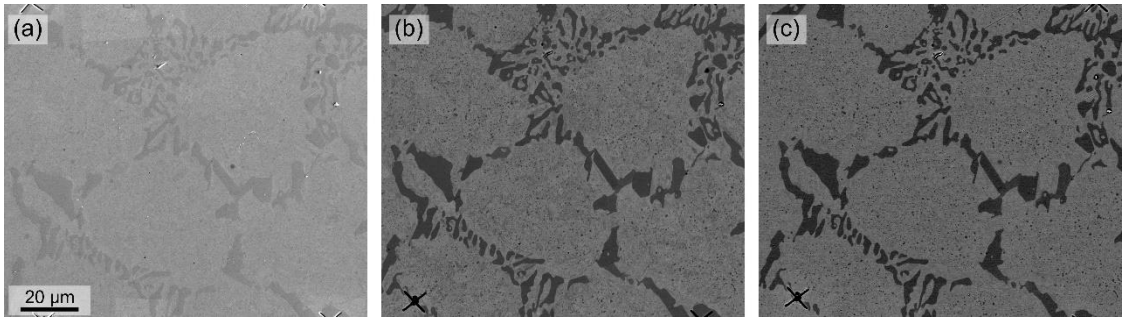

Figure 2: SEM images showing the eutectic and secondary carbides. a) SE, b) BSE and c) BSE with Au-Pt film.

Figure 2a and Figure 2 (b, c) show the secondary electron (SE) and BSE images of the same area of the sample, respectively. SEM images from secondary electron do not present sufficient contrast between matrix and carbide for the unambiguous characterization of the carbides (principally of the secondary carbides). For this reason, BSE imaging was used to identify the distribution and morphology of secondary carbides. This imaging mode shows the contrast between different phases since the information is obtained as a function of the sample chemical composition where heavier elements appear brighter than lighter elements. Furthermore, the contrast in the BSE was improved by depositing a very thin film Au-Pd layer (approx. 5 nm) using an EMITECH K950X PVD equipment. This

layer makes weaker the signal coming from the matrix and thus, the contrast effect produced by grain orientation is reduced. In this way, the carbides can be easily identified from the matrix enabling a more efficient I-A. This effect can be observed in Figure 3.

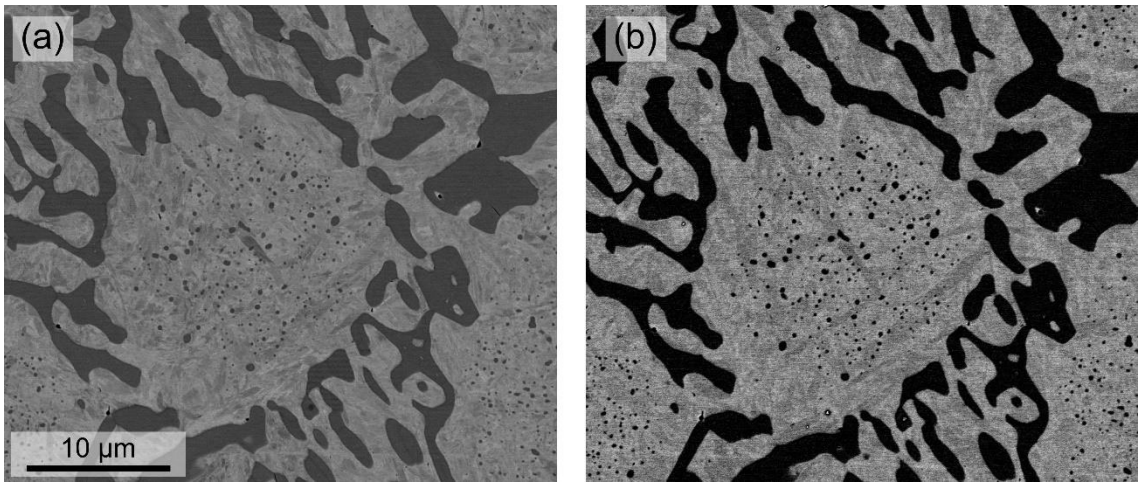

Figure 3: BSE images showing the difference contrast by adding an Au-Pd layer: a) without and b) with Au-Pd layer

It is worth to mention that the selection of the image magnification is non-trivial for an appropriate characterization of the carbides. At low magnification the secondary carbides are not well distinguished and at higher magnifications no eutectic carbides fit complete within the image, as shown in Figure 4. For this reason, and due to the difference in size between eutectic and secondary carbides, they cannot be analysed simultaneously from a same image. The focus of this work is to evaluate and characterize the secondary carbides precipitated during the thermal treatment.

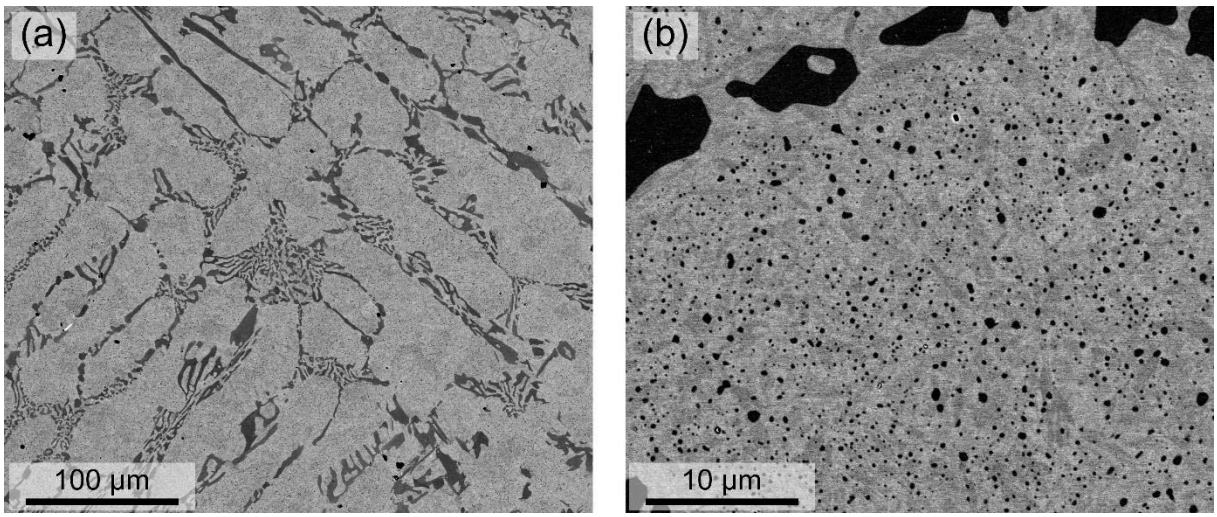

Figure 4: BSE image a) eutectic carbides are shown at low magnification (325X – horizontal field width (HFW): 394 µm) and b) secondary carbides are identified at higher magnification (3250X – HFW: 39.4 µm)

In order to evaluate the effect of depositing a Au-Pd layer in the I-A process, images of the same areas were analysed with and without the top layer. For that, three regions were delimitated by crosses made using FIB, as shown in Figure 6.

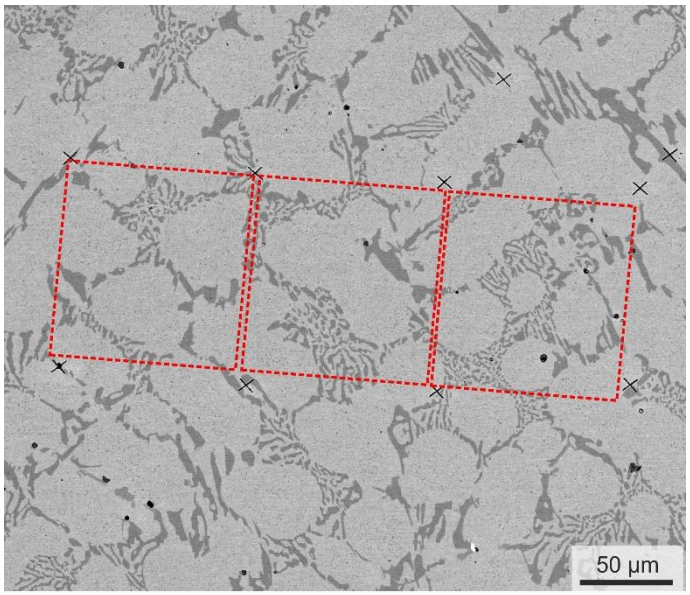

Figure 5: different areas of the samples used for the microstructural analysis.

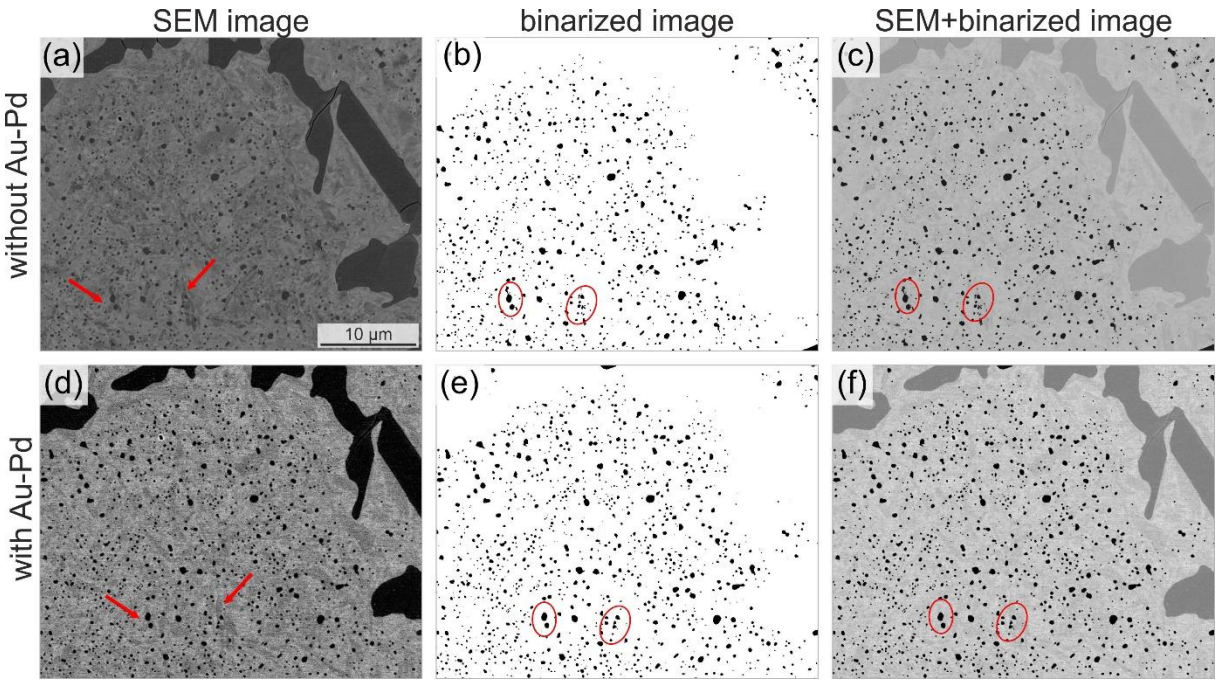

Figure 6: Comparison of IA of the samples with and without Au-Pd layer: a), d) SEM images (in BSE mode); b) binarized images and the combination of SEM+IA

Figure 6 shows a comparison after I-A of the images with and without Au-Pd layer. It can be observed in Figure 6a a strong signal coming from the matrix due to grain orientation, which can affect the analysis of the secondary carbides. The arrows (Figure 6a) indicate some areas in the sample where

high contrast is coming from the matrix and affect the posterior I-A (Figure 6b, 6c). During the binarization by threshold, these areas are considered as new particles or a part of other, resulting in error in the carbide size and area fraction occupied by them. However, in Figure 6 d the contrast effect produced by grain orientation is weaker making easier the separation of the carbides from the matrix. This is because of the Au-Pd thin film, which as mentioned before, helps to reduce the EBS signal coming from the matrix. The same regions than in Figure 6a, 6b and 6c are highlighted in Figure 6d, 6e and 6f for a direct comparison of the advantages by using a Au-Pd films in the segmentation during I-A.

Etching and CLSM

CLSM, with a Z resolution of 10 nm, was used for the topographical and morphological characterization of secondary carbides. For an optimal measurement the carbides and matrix must be localized at different height levels and as consequence, a deep etching should expose the embedded carbides by removing the matrix. Some of the secondary carbides will be removed along with the matrix during the etching, whereas new ones should appear in the surface that used to be in lower levels. Parallel plane surfaces are essential to perform accurate measurements, since it can be affected by any small tilt given the small size of the secondary carbides.

Different etching solutions were used for revealing the secondary carbides, such as Marble (8 g $CuSO_4$, 40 ml HCl, 40 ml Water), Vilella (1g picric acid, 5 ml HCl, 100 ml C_2H_6O), RNO (80 ml C_2H_6O, 10 ml HNO_3, 10 ml HCl, 1.2 g picric acid) and Murakami (10 g $K_3Fe(CN)_6$, 10 g NaOH, 100 ml Water) for times between 8-50 seconds depending on the sample and the etching solution. The best results were obtained using Vilella (10 seconds) and the corresponding CLSM images were used for the I-A and subsequent particle size determination (Figure 7).

The particle analysis (i.e. segmentation, binarization and particle parameters determination) is performed after a colour segmentation of the CSLM images (Figure 7a) by removing the matrix (green) from the carbides. The software A4i was used for the segmentation, binarization and particle size determination, whereas the Fiji software [25] was used for the near neighbour distance determination.

Some artefacts were observed during the segmentation at the border of the eutectic carbides, due to the difference in high between the centre and the border. These borders appear as new particles in the binary image of Figure 7c. However, the final average particle size and nnd is not affected as observed by analysing smaller areas which did not included eutectic carbides.

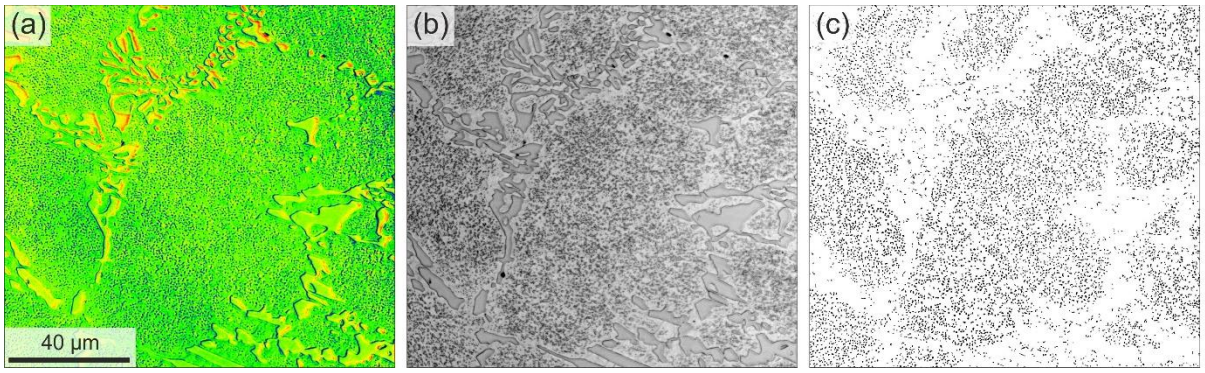

Figure 7: Samples etched with Vilella reagent for 10 seconds: a), b) CLSM images in laser and optical mode, respectively; c) binarized image from a)

2.2.- Particles analysis

The secondary carbides size and morphology were determined by performing I-A of the BSE and CLSM images using the software A4i®. For the automatic detection and analysis of the particles, an image binarization is needed, which is performed adjusting the threshold range. The result is a black-white image where the objects of interest are apart from the background. Examples of the resulting images after particle identification are shown Figure 6 and Figure 7.

3.- Results and Discussion

3.1.- Microstructure and carbides identification

The microstructure of the sample after SCD+Q treatment consist of eutectic carbides, formed during the solidification, and secondary carbides embedded in a martensitic matrix. The secondary carbides were precipitated during the austenite destabilisation at 980 °C (point 1 in Figure 1). The SCD step (point 2 in Figure 1) leads to a transformation of the matrix from austenite to ferrite. Finally, a subsequent quenching step (austenization at 980 °C and air quenched) results in a fully martensitic matrix . More details on the constituent phases can be found elsewhere [20] .

Different carbides have different response to external effects, namely: corrosion, mechanical, thermal behaviour. Their differentiation can be made, in very few cases, by morphology. However, there are certain cases in which this is not possible ($M_7C_3/M_{23}C_6$), since they might be a transitional phase that shifts between the different compositions. In the particular case of HCCI, depending on the Cr and C concentration, it is possible to obtain M23C6 carbides that are mainly differentiated from M_7C_3 by their crystallography.

3.1.1.- Chemical characteristics

EDX mapping was carried out to identify the carbides and the chemical elements forming them. The distribution of Fe, Cr and C is shown in Figure 8. Although carbon is not a heavy enough element for the EDX scans to provide useful data [9], it was also mapped for a distribution overview and for identifying the carbide distribution.

The eutectic carbides are mainly Cr-rich carbides (Cr_xC_y), as shown in Figure 8. This is inferred from the fact that the sites with the highest Cr concentrations are coincident with regions of high C and low Fe content. Secondary carbides of sub-micron size, on the contrary, are not large enough for their characterization at the used magnification (2000x).

The literature [20,26] states that the eutectic and secondary carbides present in the HCCI analysed here are of the M_7C3 type. However, to unambiguously identify the nature of the carbides other techniques such EBSD are also needed.

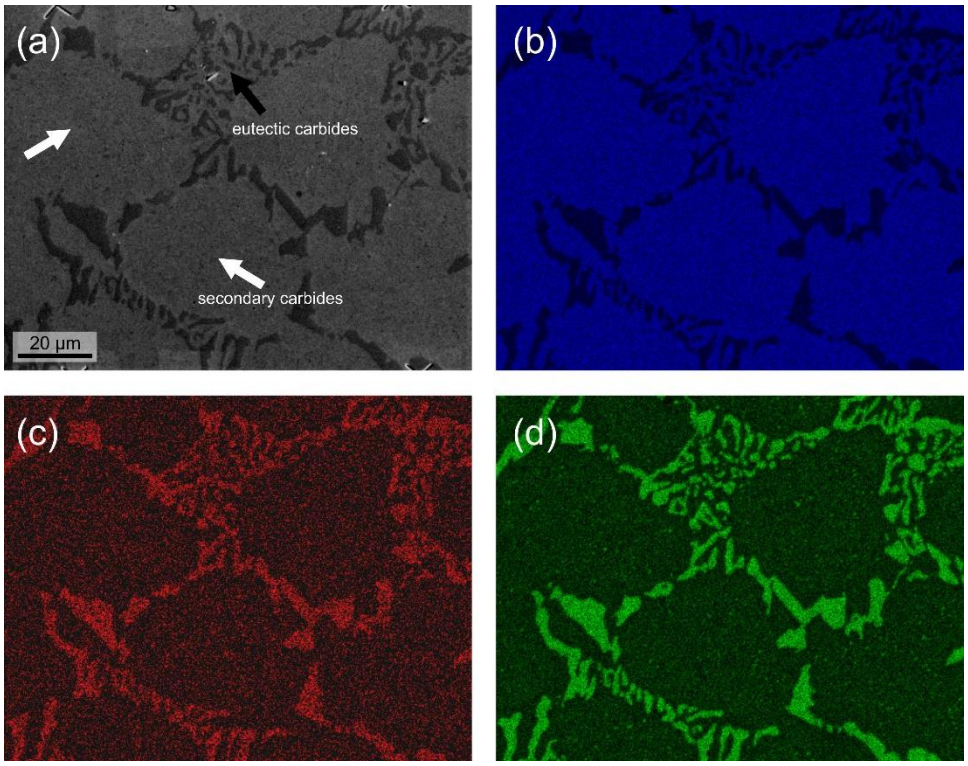

Figure 8: SEM image and EDX mapping taken at 15 KV and at a magnification of 2000X. a) SE image showing the eutectic (black arrow) and secondary carbides (white arrow); b) Fe distribution map; c) C distribution map and d) Cr distribution map.

3.1.2.- Crystallographic characteristics

Figure 9 shows the Kikuchi pattern corresponding to the secondary carbides, which were identified as the M_7C_3 type, which are essentially Cr-rich carbides with a pseudohexagonal structure [27]. The confidence index (CI) and fit parameters for both phases are 0.452 and 0.69 for the M_7C_3 phase and 0.012 and 2.13 for the $M_{23}C_6$ phase, respectively. These two parameters allow the identification of the phases evaluating the measured Kikuchi patterns against the calculated ones. The larger CI (maximum 1) and lower fit parameters (ideal value for fit = 0), the better indexing solution. For statistical reliability, more than 30 carbides were randomly measured, presenting all of them the same crystallography, as expected from data in the literature [20,26].

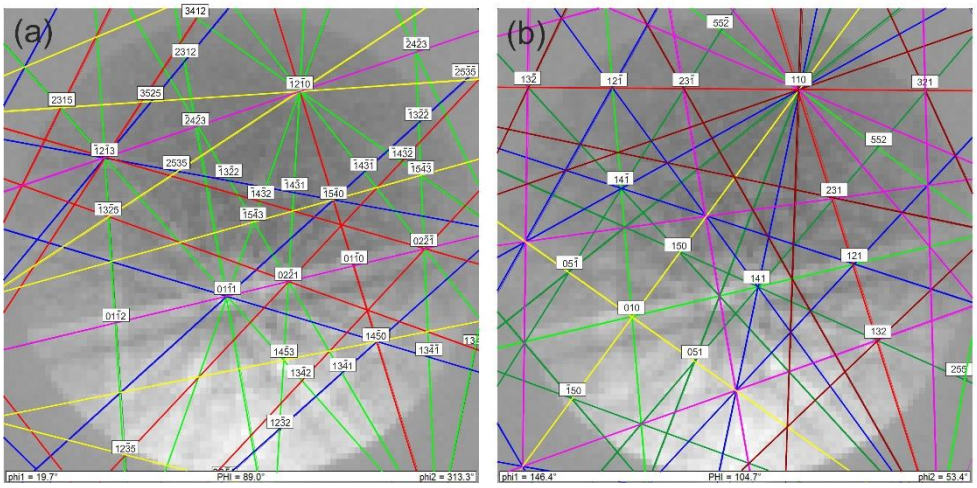

Figure 9: Kikuchi patterns corresponding to the secondary carbides a) indexed with M_7C_3 (CI: 0.452 – fit: 0.69) and b) indexed with $M_{23}C_6$ (CI: 0.012 – fit: 2.13).

A scanned area is shown in Figure 10a, where the M_7C_3 carbides (in red) and the martensitic phase (in light blue) can be clearly distinguished. The carbides precipitate mostly at boundaries showing a misorientation larger than 15°, i.e. at martensite block/package boundaries or at prior austenite grain boundaries (PAGB) (Figure 10b). The precipitation of carbides at martensite block boundaries and at PAGB in alloyed steels leads to a microstructure stabilization by avoiding or retarding the grain growth and thus, resulting in an strength-ductility improvement [4,28,29].

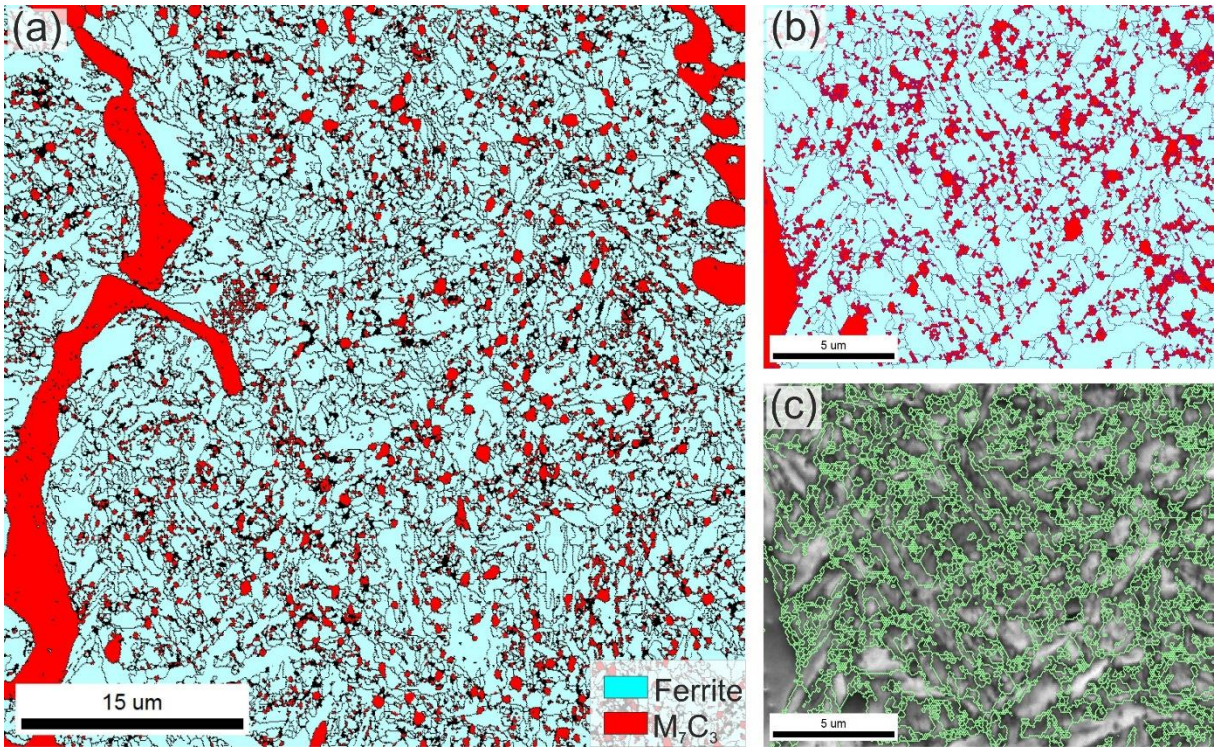

Figure 10: EBSD measurements: a) phase map showing the M_7C_3 carbides (in red) and the martensitic matrix (in light blue) using 80 nm step size. Grain boundaries with misorientation >15° are demarked with black lines; b) selected area from the phase map showing in detail the secondary carbides located at large angle boundaries (LAB) (>15°) and c) image quality map, the lines indicate the LAB.

3.2.- Secondary carbides – quantitative analysis

The secondary carbides size and morphology were determined by performing I-A of the BSE and CLSM images using the software A4i®. For the automatic detection and analysis of the particles, an image binarization is needed, which is performed adjusting the threshold range. The result is a black-white image where the objects of interest are clearly separated from the background. Examples of the resulting images after particle identification are shown Figure 6 and Figure 7.

The particle size and size distribution, the near neighbour distance, the distribution homogeneity and the aspect ratio will be calculated and evaluated by means of different characterization techniques previously described.

Particle size from image analysis from SEM/BSE images

Secondary carbides size and distribution was calculated from three different areas of BSE images (Figure 5). Three images were taken in each region and more than 2000 particles were included in the analysis. For the quantification, all the particles cutting the edges of the images were dismissed and only the secondary carbides were considered, since all the eutectic carbides observed in the image are incomplete.

Table 3: particle average size for the different regions (Fig.5) with and without Au-Pd layer calculated from BSE images

	No Au-Pd	With Au-Pd
Average	0.44 ± 0.28 µm	0.48 ± 0.30 µm
Zone_1	0.41 ± 0.22 µm	0.44 ± 0.19 µm
Zone_2	0.45 ± 0.32 µm	0.49 ± 0.30 µm
Zone_3	0.46 ± 0.29 µm	0.49 ± 0.29 µm

The values for the carbides size of the different regions and the average value for the three zones in Figure 5 are shown in Table 3. Only a slight variation in the values for the different regions is observed, indicating that the averaged particle size is homogeneously distributed within the sample and their average size is independent of the evaluated area. Additionally, it was noticed that the three-region average value is barely higher for the sample with Au-Pd sample. This results from a shift of the maximum of the size distribution towards higher particle size calculated from the images with and without Au-Pd layer, as shown in Figure 11a) and 11b). However, the difference in the average particle size (9% larger for Au-Pd images) remains within the calculation error.

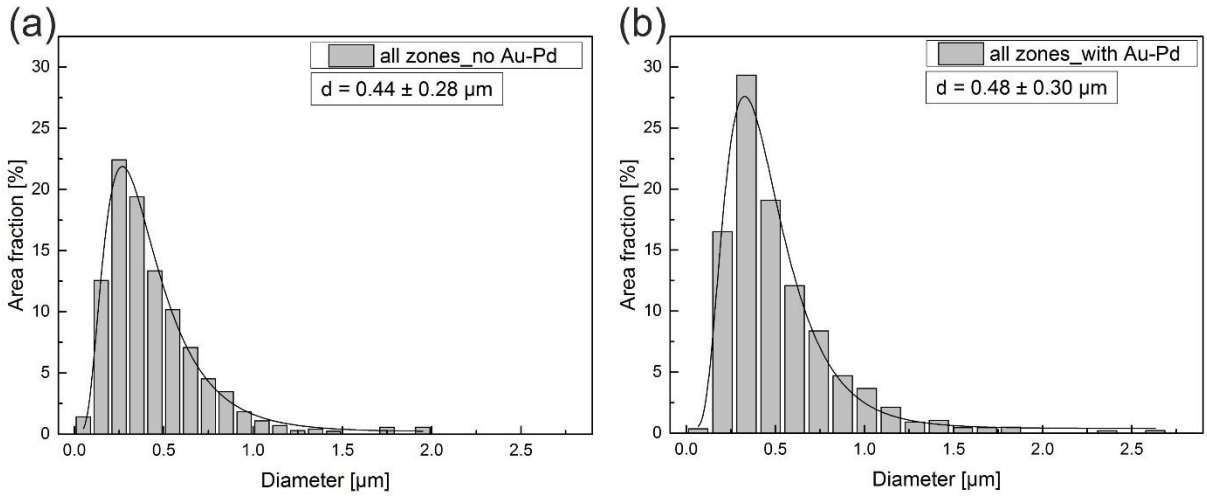

Figure 11: particle grain size distribution from BSE images: a) with and b) without Au-Pd layer at the surface

Particle size from image analysis from CLSM images

The particle size determination using CLSM images after etching was performed using three different pictures of 3 different regions of the samples. As in the case of the analysis using BSE images, all the particles cutting the edges were ignored and only the secondary carbides were considered. Figure 12 shows the carbide size distribution from the CLSM images. The particle average diameter was calculated to be 0.607 ± 0.197 µm. The difference in the mean size compared to that value from SEM images, may be due to a distortion of the apparent size of the carbides as a consequence of the topographical revealing of secondary particles together with an undesired removal of the smallest particles, which would skew the size distribution and consequently, increase the mean size value. This issue is unavoidable, since a softer etching would not reveal properly the carbides. On the other hand, if the etching is stronger, smaller particles can be easily detached from the bulk [18].

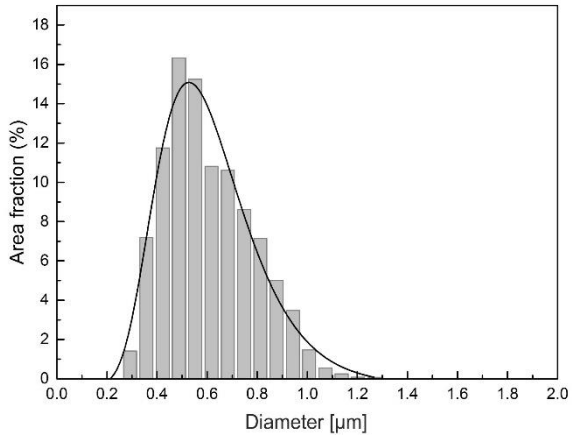

Figure 12: particle grain size distribution from CLSM images of a sample after etching with Vilella.

Particle size from EBSD measurements

A small area of the sample was scanned using 20 nm step size to show in detail the shape and distribution of the secondary carbides (Figure 13b). The particle analysis from EBSD data was

performed considering a minimum grain size of 40 nm (at least two points with the same crystallographic orientation are needed to build a grain [30]) and that valid grains must contain multiple rows. All the particles touching the edges of the image were not included in the particle size determination.

The average particle size calculated from the EBSD data was calculated to be 0.55 ± 0.32 µm and the size distribution is shown in Figure 13.

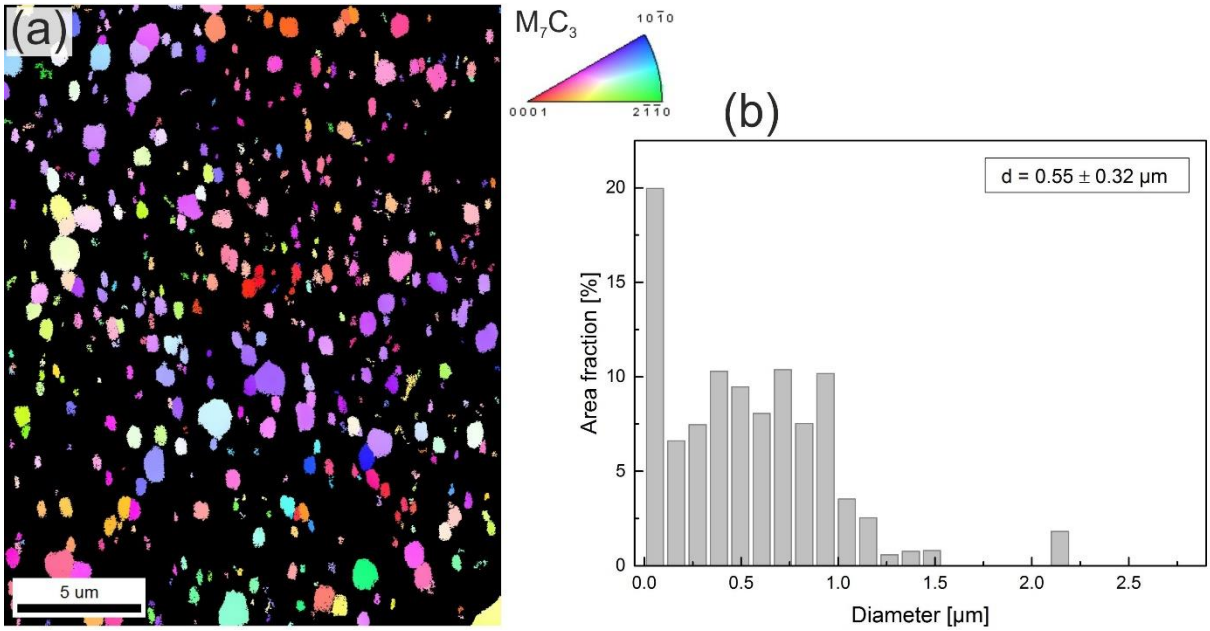

Figure 13: a) IPF map of the M_7C_3 secondary carbides using 20 nm step size; b) particle size distribution.

3.3.3.2.- Nearest neighbour distance (nnd)

The nnd was determined with the Fiji software and using a plugin [25] developed for that purpose. The nnd was calculated using the data from BSE+IA images, CLSM+IA and EBSD measurements. The *nnd* is calculated by the Fiji [25] software as the distance between the centroids of a particle and the centroid of the nearest particle. Note that the result can be biased if the size and shapes of the particles are very irregular. All the particles cutting the edges of the image were not considered for the analysis.

Distance between neighbours is considered as an important descriptive parameter to quantify the degree of distribution, since it might affect the mechanical response of the material.

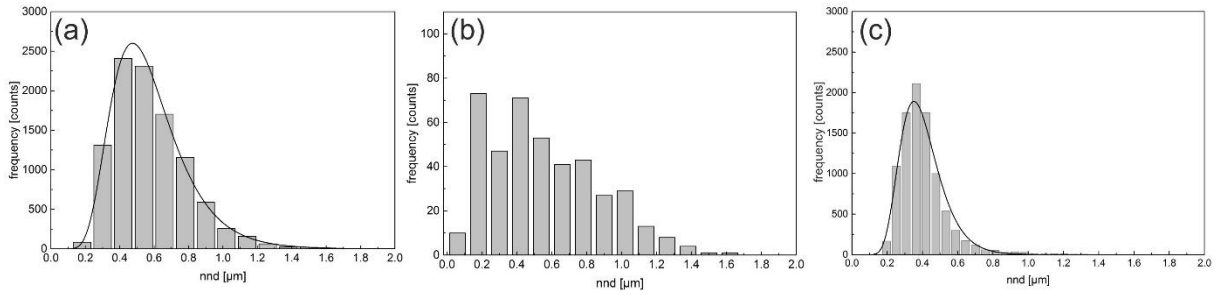

Figure 14: near neighbour distance distribution: a) from BSE images and IA; b) from EBSD IPF (Figure 13); c) from CLSM images after etching with Vilella.

The average distance between particles was calculated from BSE images to be 0.58 ± 0.25 µm. This value was calculated considering the three analysis areas (Figure 5) together. The nnd values calculated for the different regions separately do not deviate much from that value, being 0.57 ± 0.22 µm, 0.58 ± 0.27 µm and 0.61 ± 0.29, respectively.

The nnd value for the CLSM images was 0.40 ± 0.14 µm whereas from EBSD measurements the value was 0.55 ± 0.32 µm.

Attention must to be payed to the distribution of the particles for the nnd calculation. Figure 6 and Figure 7 show particles at both sides of the eutectic carbides, which might affect the nnd distribution and the average values towards larger values.

Carbide shape

Besides the size and distribution of carbides, their morphology are of significance in assessing the mechanical properties [23]. One parameter to quantify the particle morphology is the shape factor or particle aspect ratio (AR). It is defined as the ratio between wide and length of a particle, where a value of 1 corresponds to a perfect sphere. AR values and distribution determined from the different techniques are shown in Table 4 and Figure 15, respectively.

From the results it is evidenced tendency of the secondary carbides to show a round shape, since the AR values are more close to 1. AR values for the SEM (BSE) images with and without Au-Pd layer show any deviation, indicating that the Au-Pd do not introduce any microstructural modification, besides improving the contrast for the further binarization. On the other way, the AR calculated from etching+CSLM is smaller, indicating a less rounded shape of the carbides. This might be the result of an uneven etching of the matrix in the vicinity of secondary carbides or to a deeper etching in the regions where small carbides were removed.

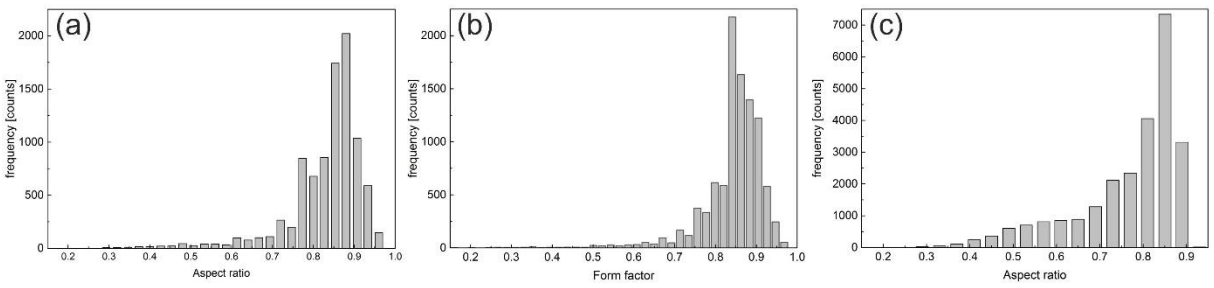

Figure 15: Particle aspect ratio distribution a) BSE+IA (no Au-Pd layer); b) BSE+IA (Au-Pd layer); c) etching+CSLM.

Table 4: Particle aspect ratio values for the different characterization techniques

	Etching+CSLM	BSE (no Au-Pd)	BSE (with Au-Pd)
Aspect Ratio	0.76 ± 0.12	0.83 ± 0.09	0.84 ± 0.08

Carbide distribution

A general idea of the carbide distribution can be obtained by the coefficient of variance. It is defined as the ratio of standard deviation to the mean value, in this particular case of the distance between the particles (nnd) [31]:

$$V(\%) = \frac{\sigma_{\mathrm{dev}}}{\overline{nnd}} x100$$

Where *V* is the coefficient of variance and its value tending to zero represents a homogeneous particle distribution, nnd is the distance between particles and σ is the standard deviation.

Table 5: nnd and coefficient of variation calculated for the different characterization methods

	Nnd [µm]	σ [µm]	*V* (%)
BSE + I-A	0.58	0.25	43.1
CLSM + I-A	0.40	0.14	35.0
EBSD	0.55	0.32	58.2

Different values for the coefficient of variation was determined for the different characterization methods used in this work (Table 5). By analysing these parameters, intent to avoid the subjective characterization and evaluation of microstructural evolution in MMC or materials with second phase precipitates.

Conclusions

Second phase particles, in form of secondary carbides, were characterized by wide span of different characterization techniques. Chemical and crystallographic identification were performed using EDS and EBSD, respectively. Particle size, distribution and morphology were determined using IA from images acquired by SEM in backscattered mode and CLSM after etching the matrix for carbides revealing.

EBS images allow the detection and analysis of the carbides by contrasting different phases as a function of the chemical composition. However, eutectic and secondary carbides present in the microstructure of HCCI are not possible to be simultaneously analysed from EBS images, due to their significant difference in size. A possible solution is proposed by stitching several images, which would result in large images with higher resolution, including a wider surface area. Furthermore, the contrast between the matrix and secondary carbides was highly improved by coating the sample with a thin layer of Au-Pd. Besides not observing any difference in the carbide size with and without Au-Pd layer, the binarization process results straightforward. This is critical for the final results since the detection of small particles using SEM/BSE + IA is highly dependent on the threshold values used during the binarization. However, it is worth to mentioning that the proposed methodology would also work without the application of this layer. The main drawback would be a more difficult binarization of the acquired images.

The best etching conditions for the CLSM were obtained by applying the Villela etchant. However, the etching time/strength is of utmost importance, since small particles might be removed during the etching process, affecting the reliable determination of the mean particle size.

Additionally, EBSD allows to identify small particles sizes when small step sizes are accordingly used during the measurement. However, this parameter delimits the total area to be scanned, resulting in a statistically limited value.

To conclude, it is worth to mention that the combination of characterization techniques shown in this work, are easily transferable to other composite materials for the evaluation of second phase particles.

Bibliography

[1] A. Sanaty-Zadeh, Comparison between current models for the strength of particulate-reinforced metal matrix nanocomposites with emphasis on consideration of Hall-Petch effect, Mater. Sci. Eng. A. 531 (2012) 112–118. doi:10.1016/j.msea.2011.10.043.

[2] D. Rojas, J. Garcia, O. Prat, C. Carrasco, G. Sauthoff, A.R. Kaysser-Pyzalla, Design and characterization of microstructure evolution during creep of 12% Cr heat resistant steels, Mater. Sci. Eng. A. 527 (2010) 3864–3876. doi:10.1016/j.msea.2010.02.056.

[3] O. Prat, J. García, D. Rojas, J.P. Sanhueza, C. Camurri, Study of nucleation, growth and coarsening of precipitates in a novel 9%Cr heat resistant steel: Experimental and modeling, Mater. Chem. Phys. 143 (2014) 754–764. doi:10.1016/j.matchemphys.2013.10.010.

[4] A.A. Barani, F. Li, P. Romano, D. Ponge, D. Raabe, Design of high-strength steels by microalloying and thermomechanical treatment, Mater. Sci. Eng. A. 463 (2007) 138–146. doi:10.1016/j.msea.2006.08.124.

[5] D.A. Porter, K.E. Easterling, Phase Transformations in Metals and Alloys, 2nd ed., Chapman & Hall, London, UK, 1992.

[6] K. Abdel-Aziz, M. El-Shennawy, A.A. Omar, Microstructural Characteristics and Mechanical Properties of Heat Treated High-Cr White Cast Iron Alloys, Int. J. Apllied Eng. Res. 12 (2017) 4675–4686.

[7] R. Song, D. Ponge, D. Raabe, Improvement of the work hardening rate of ultrafine grained steels through second phase particles, Scr. Mater. 52 (2005) 1075–1080. doi:10.1016/j.scriptamat.2005.02.016.

[8] F.J. Humphreys, M. Hatherly, Recrystallization and related annealing phenomen, Pergamon, 1996.

[9] P.J. Goodhew, J. Humphreys, R. Beanland, Electron microscopy and analysis, (2001) 265 pp. doi:10.1037/0022-006X.76.3.524.

[10] J. Fujita, N. Hemmi, S. Tohyama, T. Seki, Y. Tamura, K. Fuku, Practical Application of Confocal Laser Scanning Microscopy for Cardiac Regenerative Medicine, Confocal Laser Microsc. - Princ. Appl. Med. Biol. Food Sci. (2013) 3–18. doi:10.5772/55864.

[11] J.P. Bacon, C. Gonzalez, C.J. Hutchison, Pharmaceutical applications of Confocal Laser Scanning Microscopy, Trends Cell Biol. 1 (1991) 172–175.

[12] J.A.R. Cardona, C.H. Iriart, M.L. Herrera, Applications of confocal laser scanning microscopy (CLSM) in foods, Confocal Laser Microsc. - Princ. Appl. Med. Biol. Food Sci. (2013) 203–234. doi:dx.doi.org/10.5772/55653.

[13] M. Montoto, A. Martinez-Nistal, A. Rodriguez-Rey, N. Fernandez-Merayo, P. Soriano, Microfractography of granitic rocks under confocal scanning laser microscopy, J. Microsc. 177 (1995) 138–149. http://onlinelibrary.wiley.com/doi/10.1111/j.1365-2818.1995.tb03544.x/full.

[14] E. Merson, A. V. Kudrya, V.A. Trachenko, D. Merson, V. Danilov, A. Vinogradov, Quantitative characterization of cleavage and hydrogen-assisted quasi-cleavage fracture surfaces with the use of confocal laser scanning microscopy, Mater. Sci. Eng. A. 665 (2016) 35–46. doi:10.1016/j.msea.2016.04.023.

[15] A.J. Schwartz, M. Kumar, B.L. Adams, D.P. Field, Electron Backscatter Diffraction in Materials Science, 2nd ed., Springer, 2009. doi:10.1007/978-0-387-88136-2.

[16] C. Parish, T. Watkins, O. Rios, G. Mackiewicz-Ludtka, G. Ludtka, O. Cavin, Characterization of Retained Austenite and Carbides in Stainless Steel by Combined EBSD, EDS, and XRD, Microsc. Microanal. 17 (2011) 410–411. doi:10.1017/S1431927611002923.

[17] J. Guo, L.G. Liu, Q. Li, Y.L. Sun, Y.K. Gao, X.J. Ren, et al., Characterization on carbide of a novel steel for cold work roll during solidification process, Mater. Charact. 79 (2013) 100–109. doi:10.1016/j.matchar.2013.02.011.

[18] S. Karaqoz, H. Fischmeister, Quantitative metallography of high speed steels by SEM, Steel Res. 58 (1987) 46–51.

[19] D.B. Miracle, Metal matrix composites - From science to technological significance, Compos. Sci. Technol. 65 (2005) 2526–2540. doi:10.1016/j.compscitech.2005.05.027.

[20] M.A. Guitar, S. Suárez, O. Prat, M. Duarte Guigou, V. Gari, G. Pereira, et al., High chromium cast irons:

destabilized-subcritical secondary carbide precipitation and its effect on hardness and wear properties., J. Mater. Eng. Perform. Accepted f (2018). doi:https://doi.org/10.1007/s11665-018-3347-1.

[21] G.L.F. Powell, J. V. Bee, Secondary carbide precipitation in an 18 wt%Cr-1 wt% Mo white iron, J. Mater. Sci. 31 (1996) 707–711. doi:10.1007/BF00367889.

[22] H. Gasan, F. Erturk, Effects of a Destabilization Heat Treatment on the Microstructure and Abrasive Wear Behavior of High-Chromium White Cast Iron Investigated Using Different Characterization Techniques, Metall. Mater. Trans. A. 44 (2013) 4993–5005. doi:10.1007/s11661-013-1851-3.

[23] G.L.F. Powell, G. Laird, Structure, nucleation, growth and morphology of secondary carbides in high chromium and Cr-Ni white cast irons, J. Mater. Sci. 27 (1992) 29–35. doi:10.1007/BF00553833.

[24] Schindelin Johannes, E.F. Ignacio Arganda-Carreras, V. Kaynig, M. Longair, T. Pietzsch, S. Preibisch, et al., Fiji: an open-source platform for biological-image analysis, Nat. Methods. 9 (2012) 676–682. doi:10.1038/nmeth.2019.

[25] Y. Mao, "Nearest Neighbor Distances Calculation with ImageJ", https://icme.hpc.msstate.edu/mediawiki/index.php/Nearest_Neighbor_Distances_Calculation_with_ImageJ, (n.d.).

[26] S.D. Carpenter, D. Carpenter, X-ray diffraction study of M7C3carbide within a high chromium white iron, Mater. Lett. 57 (2003) 4456–4459. doi:10.1016/S0167-577X(03)00342-2.

[27] B.A. Senior, A critical review of precipitation behaviour in 1CrMoV rotor steels, Mater. Sci. Eng. 103 (1988) 263–271. doi:10.1016/0025-5416(88)90516-2.

[28] M. Asadi Asadabad, S. Kheirandish, A.J. Novinrooz, Microstructural and mechanical behavior of 4.5Cr-2W-0.25V-0.1C steel, Mater. Sci. Eng. A. 527 (2010) 1612–1616. doi:10.1016/j.msea.2009.10.042.

[29] V.H. Baltazar Hernandez, S.S. Nayak, Y. Zhou, Tempering of martensite in dual-phase steels and its effects on softening behavior, Metall. Mater. Trans. A Phys. Metall. Mater. Sci. 42 (2011) 3115–3129. doi:10.1007/s11661-011-0739-3.

[30] S. Suwas, R.K. Ray, R.K.R. Satyam Suwas, Crystallographic Texture of Materials, 2014. doi:10.1007/978-1-4471-6314-5.

[31] S.-T. Oh, T. Sekino, K. Niihara, Effect of particle size distribution and mixing homogeneity on microstructure and strength of alumina/copper composites, Nanostructured Mater. 10 (1998) 327–332. doi:10.1016/S0965-9773(98)00072-5.